Int. J. Electrochem. Sci., 8 **(2013)** 10540 - 10548

International Journal of
ELECTROCHEMICAL
SCIENCE
www.electrochemsci.org

High Rate Capabilities Fe-doped EMD Electrodes for Li/MnO_2 Primary Battery

Qiuling Liu, Shengping Wang[*], *Hong Cheng*

Faculty of Material science and Chemistry, China University of Geosciences, Wuhan 430074, PR China
[*]E-mail: robert@cug.edu.cn

Received: 11 June 2013 / *Accepted:* 6 July 2013 / *Published:* 1 August 2013

Fe_2O_3 doped MnO_2 (Fe-HEMD) with various mole percents had been synthesized via a simple solid-state synthesis using electrolytic manganese dioxide (EMD). Structure and morphology of synthesized materials were characterized by X-ray diffraction and scanning electron microscope, respectively. The XRD results revealed that anisotropic changes were occurred in the lattice parameters of Fe-HEMD, demonstrating that Fe was doped into MnO_2 materials. Electrochemical performances were evaluated by cyclic voltammetry, electrochemical impedance spectroscopy and galvanostatic discharge test. The 6 mol % Fe-doped MnO_2 (Fe-HEMD-6) electrode exhibited an excellent discharged capacity of 164.9 mAh g^{-1}, which was increased by 7.5% compared with Fe-HEMD-0 at a large discharge current density of 2.0 mA cm^{-2}. The enhanced high rate capability of Fe-HEMD-6 can be attributed to anisotropic changes of lattice parameters.

Keywords: Fe-doped; anisotropy; high-rate; Li/MnO_2 primary battery

1. INTRODUCTION

With the advantages of natural abundance, environmental benignity, cost efficiency[1] etc., manganese dioxide is widely used in alkaline zinc manganese dioxide battery [2, 3], supercapacitor [4, 5], especially in Li/MnO_2 dioxide battery [6]. Although with advantages of high nominal voltage (3 V) [7], high energy density (230 Wh Kg^{-1}), and long storage life (over 10 years, self-discharge less than 1% yearly) [8], the poor high-rate discharge ability of Li/MnO_2 dioxide battery hinders its wide application in some areas where need higher power outputs [9, 10]. Aiming at improving the high-rate discharge performance of Li/MnO_2 battery, many attempts have been made to modify the micro-structure of the manganese dioxide, such as preparing modified porous materials[11, 12], nano materials [7], lithiation treatment [13], coating [14] etc.

Generally, Li/MnO_2 primary battery employs electrolytic manganese dioxide (EMD) which needs heat treated [15, 16] before assembled battery as its cathode material to modify the structure of MnO_2 to improve its electrochemical capacity. EMD, mainly γ-MnO_2, can be considered as a random intergrowth of pyrolusite (β-MnO_2) blocks within a ramsdellite [17] (Fig. 1). Once heated, water bound to surface sites, structural water on or near the surface and bulk hydroxyl groups will be removed[13, 16], which is benefit for Li^+ diffusion at discharge progress. Some of γ-MnO_2 will gradually change to β-MnO_2 at the same time, resulting the mixture of ramsdellite and β-MnO_2. When reached 65-85 wt% of β-MnO_2, HEMD exhibits optimal electrochemical activities [18]. This paper also focuses on β-MnO_2 crystal phase. According to the reported literatures [19-23], the reduction mechanism of the Li/MnO_2 battery was as follows: Firstly, Li^+ from the electrolyte migrates into the [1×1] tunnel of β-MnO_2, and form chemical bond with O^{2-}. Then the Li^+ migrates in the [1×1] tunnel, from one O^{2-} to another adjacent O^{2-} in MnO_2 lattices to complete the transport process. Obviously, the diameter of the tunnel seriously affects the diffusion rate of Li^+ in the one-dimensional tunnel. And it does requisite to improve the high-rate discharge performance of MnO_2 by ameliorating the microstructure of MnO_2.

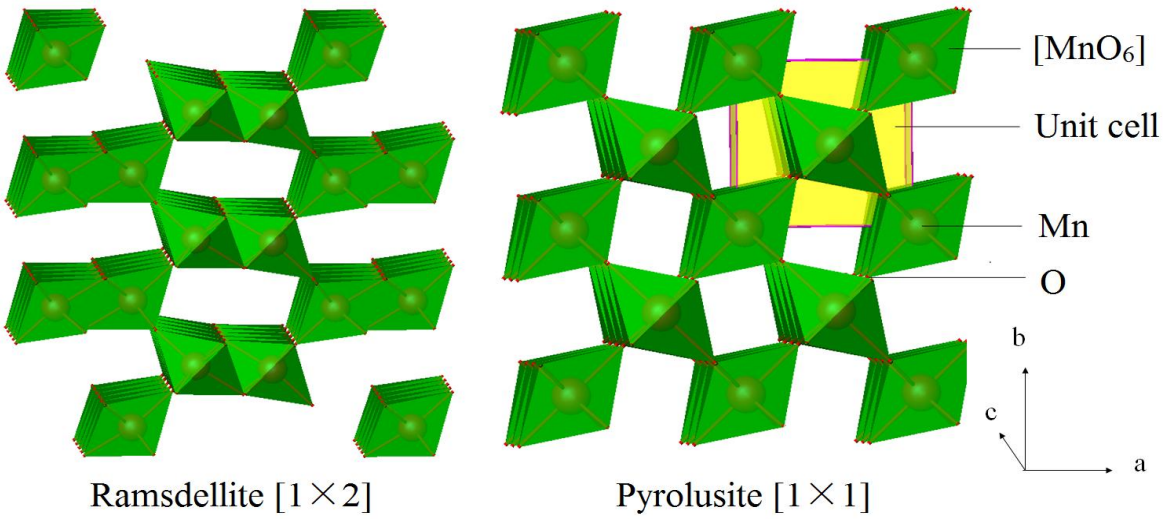

Figure 1. Structures of ramsdellite and pyrolusite-MnO_2.

For the past few years, researchers have been focusing on doping different metal cations into the MnO_2 matrix to better the microstructure of MnO_2, such as Mg and Ba [24], Ti [25], V [26], Cr [27], Bi [28], Sn [29], Ce [30] etc. In this paper, we adopted a simple way to synthetize Fe_2O_3 doped EMD (Fe-HEMD). The doping Fe element can expand Li^+ diffusion channel and shorten the migration path in the MnO_2, thereby weakening the polarization in solid phase caused by Li^+ diffusion and further improving high-rate discharge performance for Li/MnO_2 battery.

2. EXPERIMENTAL

EMD (Xiangtan. China) was mixed with 0 mol %, 3 mol %, 6 mol %, 9 mol % Fe_2O_3 (AR) respectively. After grinding 20 min in an agate mortar, the samples were heated in a muffle furnace at a rate of 5 °C min^{-1} to 375 °C and last for 10 h. Fe-doped MnO_2 were obtained, denoted as Fe-HEMD-0, Fe-HEMD-3, Fe-HEMD-6 and Fe-HEMD-9, respectively.

Fe-HEMD samples were characterized by X-ray diffraction patterns (Bruker/D8-FOCUS, Germany) with a Cu Kα radiation source with a beam voltage of 40 kV and a 100 mA beam current. The scan angle was set at 20–70° with a 6° min^{-1} rate of analysis. The result of lattice parameters based on XRD data was calculated by jade 5.5. The morphologies were observed with scanning electron microscope (Hitachi/SU8081. Japan).

Electrochemical simulated cells were employed to measure the electrochemical properties. The prepared powders were mixed with 5 wt % of graphite, 5 wt % of acetylene black and 5 wt % of polyvinylidene fluoride binder in N-methyl-2-pyrrolidone to produce a homogeneous paste. Then the resulting mixture was coated onto one side of aluminum foil by a coater（MTI. China), then dried at 80 °C for 24 h. The simulated cells were assembled in a argon atmospheric glove box (Labstar1800/780. Germany), with a disk-like pellet (of 15 mm diameter, 60 μm thickness and 6 mg weight) as the cathode, lithium metal as the anode, Celgard2400 as the separator and 1 M $LiClO_4$/PC+DME+DIOX(1:1:1, vol %) as electrolyte. The cyclic voltammetry test was carried out between 2.0 V and 4.0 V at 0.5 mV s^{-1} and electrochemical impedance spectroscopy was carried out by applying an ac signal with amplitude of 5 mV at the frequency varying from 50 mHz to 1 kHz at an open circuit voltage (OCV) by VMP3 electrochemical workstation (Biologic. France). The galvanostatic discharge current densities were 0.1 mA cm^{-2} and 2.0 mA cm^{-2} with 2.0 V cutoff voltage by BT2000 battery test equipment (Arbin. USA).

3. RESULTS AND DISCUSSION

3.1 XRD

The XRD patterns of as-prepared Fe-HEMD samples is shown in Fig. 2. The bottom XRD pattern represents standard XRD pattern of Fe_2O_3. Peaks appear at about 37.1°, 42.4° and 56.2° are corresponded to γ-MnO_2 phase. Broad peak 28.6° belongs to the characteristic peak of pyrolusite MnO_2 (PDF#24-0735). It suggests that the prepared Fe-HEMD samples are mixed crystal phase of γ-MnO_2 and β-MnO_2, and the doped Fe_2O_3 has not changed the crystal forms of MnO_2. There is no visual indication of additional phases for no extra peaks observed. Compared with standard XRD pattern of Fe_2O_3, peaks (2θ = 24.1°, 33.1°, 35.6°, 40.8°, 49.5°, 54.1°, 57.5°, 62.5°, 64.0°) of Fe_2O_3 doped in MnO_2 increase with increasing content of Fe_2O_3. This indicates that the Fe-HEMD samples are not pure because of the excessive dopant.

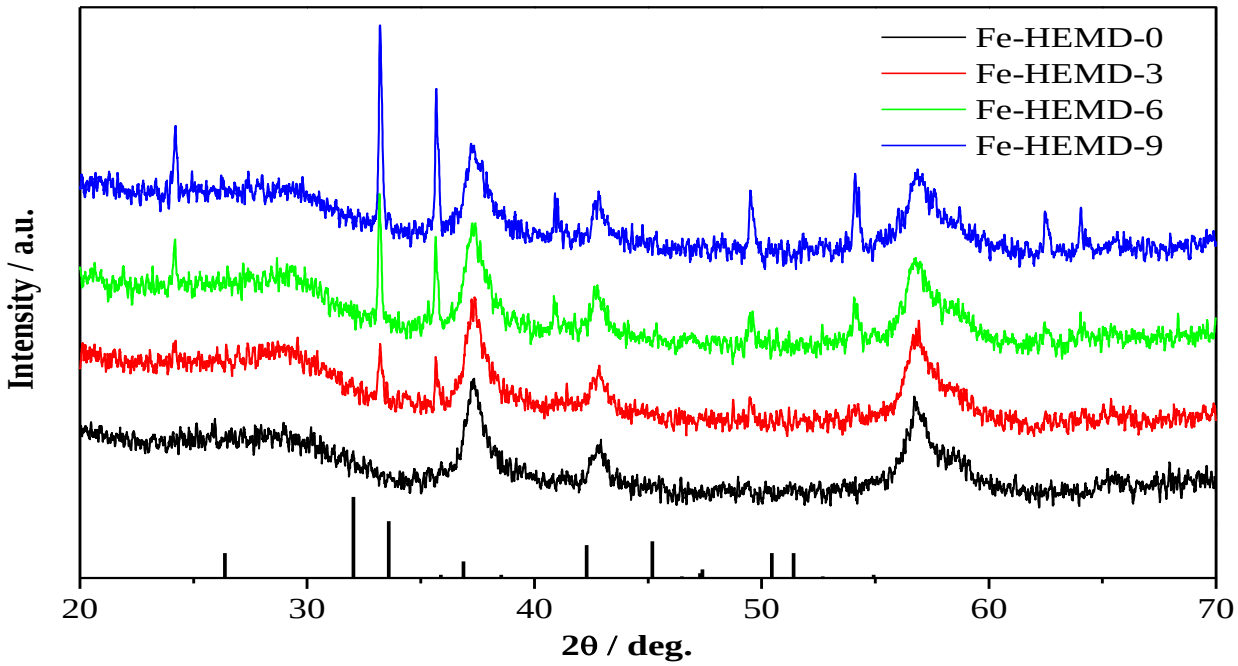

Figure 2. XRD diffraction patterns of the Fe-HEMD samples. The vertical line at the bottom is standard XRD pattern of Fe_2O_3 (PDF#33-0664).

Crystal lattice parameter refinement results for β-MnO_2 of four samples are shown in Table 1. The refined unit cell parameters (Table 1) are consistent with a = 4.418 *Å*, and c = 2.877 *Å* values obtained by pyrolusite MnO_2 (PDF#24-0735). It is interesting to note that the anisotropic changes of lattice parameters occurred in Fe-doped MnO_2, indicating that some Fe_2O_3 are doped into MnO_2 structure. Fe-HEMD-3 and Fe-HEMD-6 present the results of increased *a*-value and decreased *c*-value, while the *V* of Fe-HEMD-3 is decreased, and which of Fe-HEMD-6 is increased. And *a* increased, *c* and *V* decreased in Fe-HEMD-9, these are probably influenced by the excess Fe_2O_3.

Table 1. The calculated lattice parameters for β-MnO_2 of Fe-HEMD.

Samples	*a(Å)*	*b(Å)*	*c(Å)*	*V(Å^3)*
Fe-HEMD-0	4.3859	4.3859	2.8852	55.500
Fe-HEMD-3	4.3929	4.3929	2.8710	55.403
Fe-HEMD-6	4.4206	4.4206	2.8765	56.212
Fe-HEMD-9	4.3373	4.3373	2.9070	54.687

3.2 SEM

The SEM micrographs of four samples of Fe-HEMD are shown in Fig. 3. All samples are small particles and distribute homogeneously. Fe-doped MnO_2 samples agglomerate slightly, and the

morphologies have no obvious difference. The result shows that the doped Fe_2O_3 almostly have negligible effect on the morphology of HEMD.

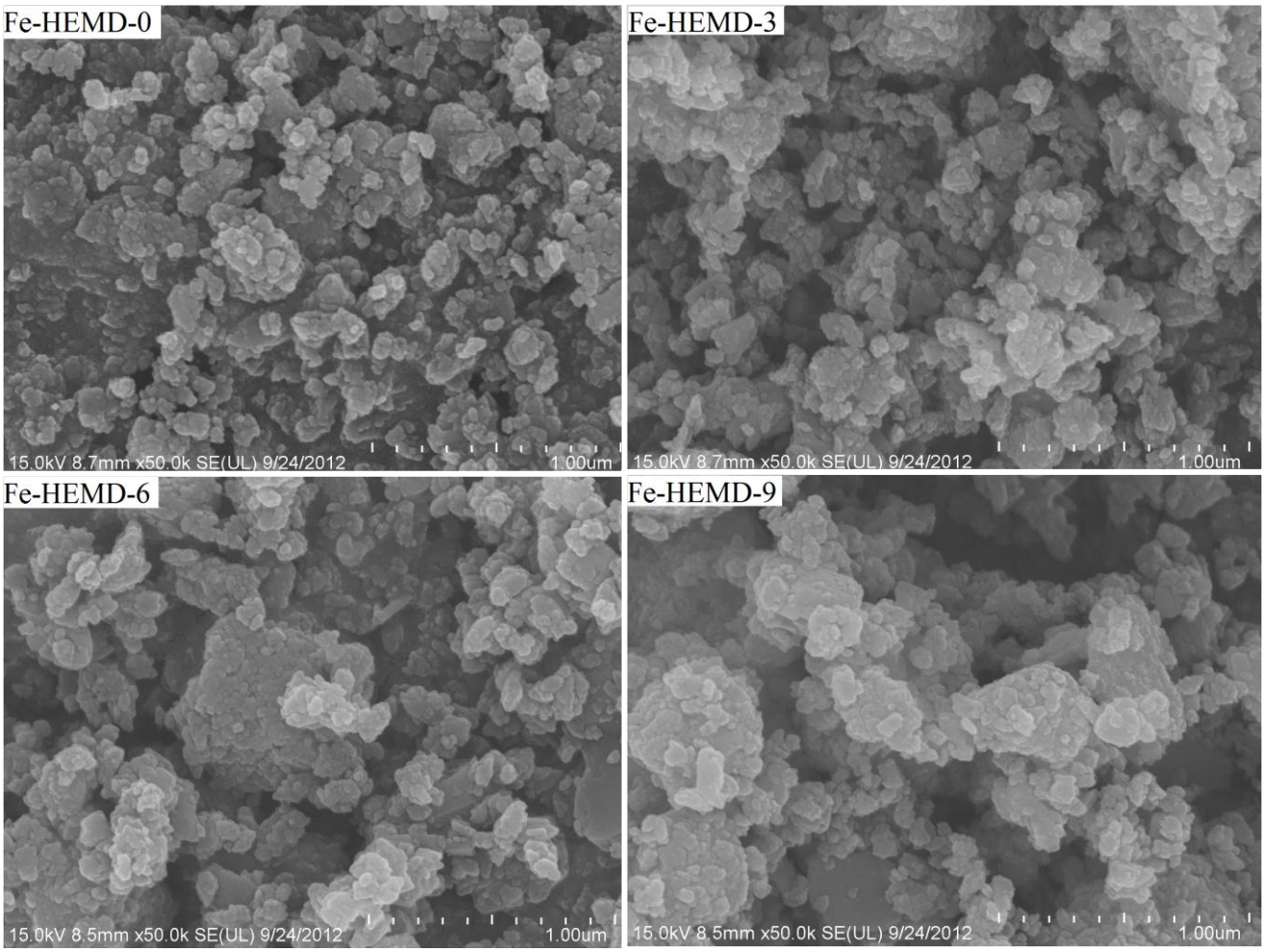

Figure 3. SEM micrographs of the Fe-HEMD samples.

3.3 Electrochemical performances

3.3.1 Cyclic voltammetry

The CV plots of Fe-HEMD samples at a scanning rate of 0.5 mV s^{-1} are illustrated in Fig. 4. It can be seen that Fe-HEMD-6 shows the largest reduction peak current compared with others. This can be attributed to its larger *a* and shorter *c*. The enlarged *a* enlarges the Li^+ diffusion cross section of MnO_2 matrix more easily and reduces the polarization caused by Li^+ diffusion. The redox potential separation of all Fe-doped samples are lower than Fe-HEMD-0, implying that electrode reversibility are improved.

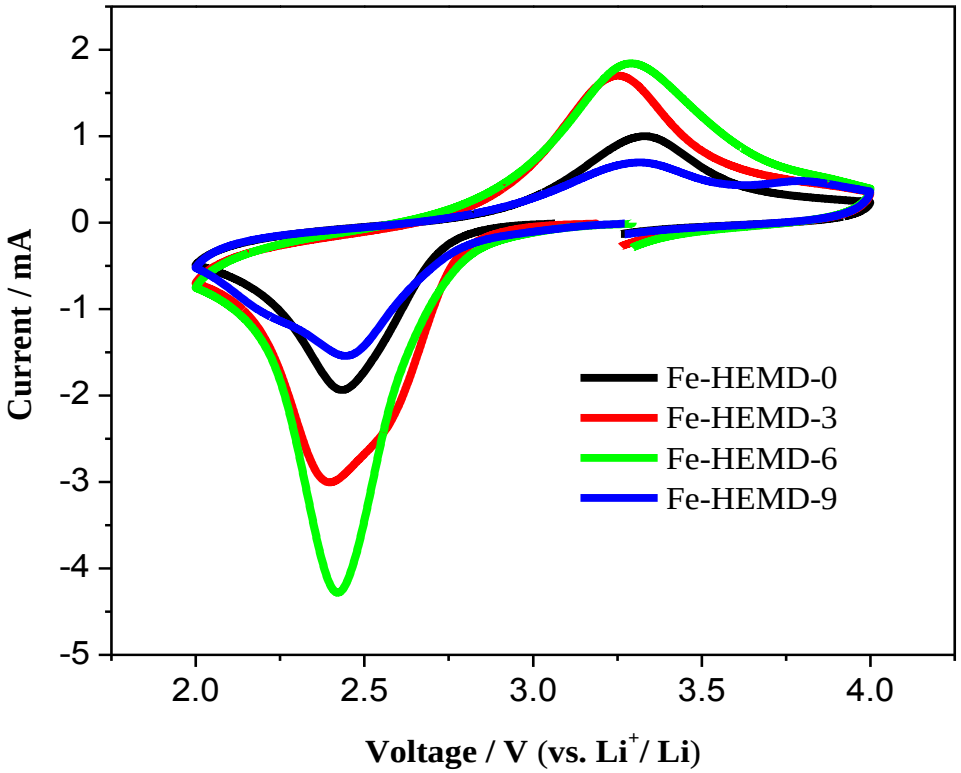

Figure 4. Cyclic voltammogram plots of the Fe-HEMD samples at a scanning rate of 0.5 mV s^{-1}

In the XRD diffraction patterns of Fe-HEMD samples, peaks of Fe_2O_3 are obvious, but in the cyclic voltammogram plots, the oxidation and reduction peaks owning to Fe_2O_3 are not found. This indicates that Fe_2O_3 is not involved in the redox reaction within the scanning voltage range.

3.3.2 Electrochemical impedance spectroscopy

Fig. 5 shows the equivalent circuit diagram and typical nyquist plots of Fe-HEMD samples. The high frequency range appears as a semicircle indicating the resistances of Li^+ embedding impedance. The low frequency range appears as a line indicating the Li^+ diffusion impedance in the solid phase of the active material. A simple equivalent circuit model [31, 32] (inset of Fig. 5) is built to analyze the impedance spectra of the three samples. In the equivalent circuit diagram, R_1 represents the ohmic resistance of the electrode system, including the electrolyte and the cell components. R_2, R_3 represent the charge transfer resistance. Q is a constant phase angle element, represent the double layer capacitance. R_2/Q_2 represents the surface layer of MnO_2 in contact with electrolyte. R_3/Q_3 represents the electric double layer between solid electrolyte interphase and the active material. W is Warburg impedance, represents diffusion impedance of Li^+ in the lattice of MnO_2. Based on the equivalent circuit diagram, we use ZSimpwin software to fit the impedance spectroscopy, the electrochemical transfer impedances of Fe-HEMD-0, Fe-HEMD-3, Fe-HEMD-6, Fe-HEMD-9 are 49.63, 25.91, 22.37

and 28.09 Ω, respectively. These show that the doped Fe_2O_3 can reduce charge transfer impedance significantly, and Fe-HEMD-6 has the minimum charge transfer impedance.

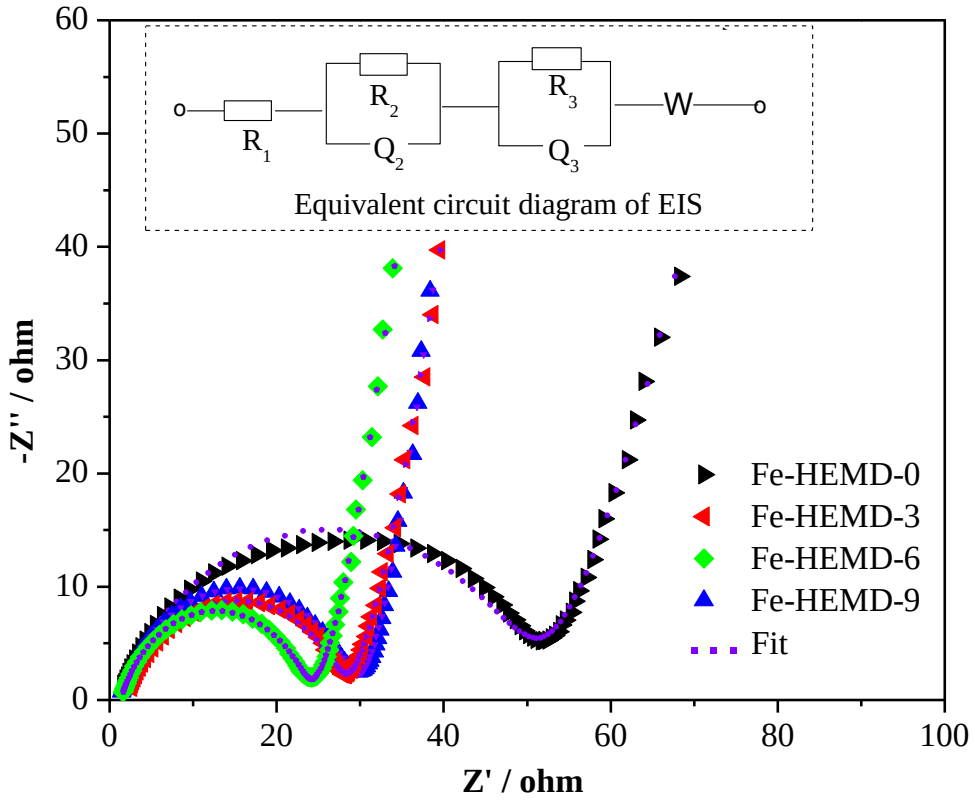

Figure 5. Equivalent circuit diagram and typical nyquist plots of Fe-HEMD samples at an open circuit potential (3.3 V vs. Li/Li^+) within a frequency range from 50 mHz to 1 kHz.

3.3.3 Galvanostatic discharge test

The discharge curves of MnO_2 electrodes at 0.1, 2.0 mA cm^{-2} with 2.0 V cutoff voltage are shown in Fig. 6. All the sample electrodes exhibit excellent specific capacity within 216-247 mAh g^{-1} at 0.1 mA cm^{-2}, in which HEMD shows the highest capacity of 247 mAh g^{-1}, indicating that doped Fe_2O_3 can't effectively improve the specific discharge capacity of MnO_2 at low discharge current density. Although the capacity of Fe doped MnO_2 are lower than undoped one at 0.1 mA cm^{-2}, a most exciting observation is that the Fe-HEMD-6 reveals the outstanding capacity of 164.9 mAh g^{-1} at current density of 2.0 mA cm^{-2}, which is increased by 7.5% comparing with undoped HEMD (153.4 mAh g^{-1}). This sensational result clarifies that the 6 mol % Fe-doped MnO_2 can do benefit for the discharge capacity of MnO_2 at high power output.

It is the anisotropic expansion (*a* increased, *c* decreased and *V* increased) in Fe-HEMD-6 bettered the rate capability of Fe-HEMD-6 [26]. The enlarged *a* enlarged the Li^+ diffusion cross section. The shorted *c* can decrease the effective diffusion path. The expanded *V* increased the effective space for insertion and extraction of Li.

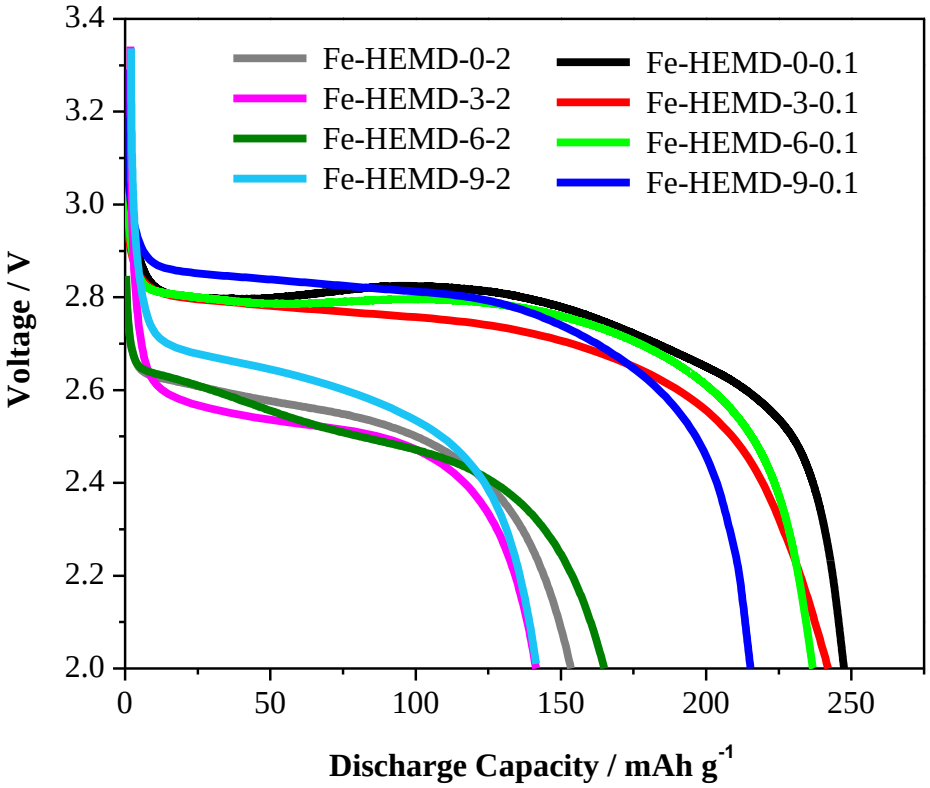

Figure 6. Discharge curves of the Fe-HEMD at 0.1mA cm^{-2} and 2.0 mA cm^{-2} with 2.0 V cutoff voltages.

At low discharge current density, Li^+ from electrolyte diffuses to the tunnels of MnO_2 orderly and further storing deep in the bulk phase. At a high discharge current density, a large number of Li^+ try to embed in the MnO_2 lattice but accumulate on the electrode interface, because the diffusion cross section of [1×1] tunnel is not broad enough. As a result, hindering Li^+ embed in MnO_2 lattice. And charge transfer polarization occurred because of the accumulated Li^+ on the surface. With the increase of depth of discharge, the embeded Li^+ diffuses into the structure of MnO_2 and combines with O^{2-} at a certain site, finally stopped. It is obvious that the shortened *c* shortens the diffusion path, and promoting Li^+ move to the destination efficiently.

4. CONCLUSIONS

In this paper, Fe-doped HEMD are prepared by a simple way using solid-state synthesis. The doping of Fe can not enhance the discharge capacity of MnO_2 material at low discharge rate (0.1 mA cm^{-2}). While it can effectively improve the Li-storage in MnO_2 at a high discharge rate (2 mA cm^{-2}), in which Fe-HEMD-6 electrodes exhibit the best capacity of 164.6 mAh g^{-1}. This can be attributed to anisotropic changes of the lattice parameters by enlarging the Li^+ diffusion cross section, facilitating Li^+ diffusion from the outer sites to inner sites within the lattice of β-MnO_2, shortening the Li^+ migration path and increasing space to accommodate more Li^+.

ACKNOWLEDGEMENTS
We thank the financial support of the National Natural Science Foundation of China (21173198).

References

1. Q. Li, Z.L. Wang, G.R. Li, R. Guo, L.X. Ding and Y.X. Tong, *Nano. Letters*, 12 (2012) 3803-3807.
2. M. Minakshi, *J. Solid State Electrochem.*, 13 (2009) 1209-1214.
3. M. Minakshi and P. Singh, *J. Solid State Electrochem.*, 16 (2012) 2227-2233.
4. Z. Song, W. Liu, M. Zhao, Y. Zhang, G. Liu, C. Yu and J. Qiu, *J. Alloys. Compd.*, 560 (2013) 151-155.
5. C. Shen, X. Wang, S. Li, J.g. Wang, W. Zhang and F. Kang, *J. Power Sources*, 234 (2013) 302-309.
6. W.M. Dose and S.W. Donne, *J. Power Sources*, 221 (2013) 261-265.
7. A. Pendashteh, M.F. Mousavi, M.A. Kiani, S.H. Kazemi and M.S. Rahmanifar, *J. Iranian Chem. Soc.*, 9 (2012) 389-395.
8. D. Linden and T.B. Reddy, Handbook of Batteries, McGraw-Hill, New York, (2002).
9. M.S. Park and W.Y. Yoon, *J. Power Sources*, 114 (2003) 237-243.
10. Y. Yang, L. Xiao, Y. Zhao and F. Wang, *Int. J. Electrochem. Sci*., 3 (2008) 67-74.
11. X.K. Huang, D.P. Lv, Q.S. Zhang, H.T. Chang, J.L. Gan and Y. Yang, *Electrochim. Acta.*, 55 (2010) 4915-4920.
12. J.G. Wang, Y. Yang, Z.H. Huang and F.Y. Kang, *J. Power Sources*, 204 (2012) 236-243.
13. W.M. Dose, J. Lehr and S.W. Donne, *Mater. Res. Bull*., 47 (2012) 1827-1834.
14. M.J. Zhi, A. Manivannan, F.K. Meng and N.Q. Wu, *J. Power Sources*, 208 (2012) 345-353.
15. Y. Shao-Horn, S.A. Hackney and B.C. Cornilsen, *J Electrochem. Soc*., 144 (1997) 3147-3153.
16. W.M. Dose and S.W. Donne, *J Electrochem. Soc*., 158 (2011) A1036-A1041.
17. K. Chen, Y.D. Noh, K. Li, S. Komarneni and D. Xue, *J. Phys. Chem*. C, 117 (2013) 10770-10779.
18. S. Jouanneau, A. Le Gal La Salle and D. Guyomard, *Electrochim. Acta*., 48 (2002) 11-20.
19. T. Ohzuku, M. Kitagawa and T. Hirai, *J. Electrochem. Soc.*, 136 (1989) 3169-3174.
20. T. Ohzuku, M. Kitagawa and T. Hirai, *J. Electrochem. Soc*., 137 (1990) 769-775.
21. T. Ohzuku, M. Kitagawa and T. Hirai, *J. Electrochem. Soc*., 137 (1990) 40-46.
22. Y. Shao-Horn, S.A. Hackney and B.C. Cornilsen, *J. Electrochem. Soc*., 144 (1997) 3147-3153.
23. S. Sarciaux, A.L. La Salle, A. Verbaere, Y. Piffard and D. Guyomard, *J. Power Sources*, 81 (1999) 661-665.
24. M. Minakshi, M. Blackford and M. Ionescu, *J. Alloys. Compd*., 509 (2011) 5974-5980.
25. L. Binder, W. Jantscher, F. Hofer and G. Kothleitner, *J. Power Sources*, 70 (1998) 1-7.
26. S. Wang, Q. Liu, J. Yu and J. Zeng, *Int. J. Electrochem. Sci*., 7 (2012) 1242-1250.
27. X.Y. Zhan, J.J. Tang, Z.H. Li, D.S. Gao, P. Chen and Q. Wu, *J. Solid State Electrochem*., 14 (2010) 1007-1011.
28. M. Minakshi, *J. Solid State Electrochem.*, 13 (2009) 1209-1214.
29. A.M. Hashem, H.M. Abuzeid, A.E. Abdel-Ghany, A. Mauger, K. Zaghib and C.M. Julien, *J. Power Sources*, 202 (2012) 291-298.
30. M. Minakshi, K. Nallathamby and D.R.G. Mitchell, *J. Alloys. Compd*., 479 (2009) 87-90.
31. F. Artuso, F. Bonino, F. Decker, A. Lourenco and E. Masetti, *Electrochim. Acta*, 47 (2002) 2231-2238.
32. J. Yan, Z. Fan, T. Wei and M. Zhang, *J Mater.Sci. Mater. Electron*., 21 (2010) 619-624.